

The effects of field line curvature (FLC) scattering on ring current dynamics and ionospheric electrodynamics

Yiqun Yu¹, Xingbin Tian¹, and Vania K. Jordanova²

¹Beihang University

²LANL

November 22, 2022

Abstract

In the ring current dynamics, various loss mechanisms contribute to the ring current decay, including the loss to the upper atmosphere through particle precipitation. This study implements the field-line curvature (FLC) scattering mechanism in a kinetic ring current model and investigates its role in precipitating ions into the ionosphere. The newly included process is solved via a diffusion equation in the model with associated pitch-angle dependent diffusion coefficients. The simulation results indicate that (1) the FLC scattering process exert mostly on energetic ions above 30 keV on the nightside where the magnetospheric configuration is more stretching. Such ion loss thereafter leads to a faster recovery of the ring current. (2) The FLC-associated ion precipitation mainly occurs in the outer region ($L > 5$ for protons and $L > 4.5$ for oxygen ions) on the nightside, and the oxygen ion precipitation takes places in a wider region than protons although its intensity is much lower. Comparisons with POES observations suggest that more precipitation is needed in the inner region, implying that other loss process is required in the model. (3) We further found that the precipitating energy flux of protons due to the FLC scattering can sometimes become comparable to the one from the electrons on the nightside, although electrons usually dominate the ionospheric energy deposit from the midnight eastward towards the dayside. (4) Finally, the FLC scattering process seems to be capable of explaining the formation of the isotropic boundary in the ionosphere.

1 **The effects of field line curvature (FLC) scattering on ring current**
2 **dynamics and ionospheric electrodynamics**

3 **Yiqun Yu^{1,2}, Xingbin Tian¹, Vania Jordanova³**

4 ¹School of Space and Environment, Beihang University, Beijing, China

5 ²Key Laboratory of Space Environment Monitoring and Information Processing, Ministry of Indus-
6 try and Information Technology, Beijing, China

7 ³Space Science and Application, Los Alamos National Laboratory, Los Alamos, NM, USA

9 **Key Points:**

- 10 • Ion precipitation associated with FLC scattering is confined outside L=5; additional scattering
11 process is needed in the inner zone
- 12 • This process contributes significantly to the ring current decay; it can explain the formation
13 of isotropic boundary
- 14 • The precipitating energy flux of protons due to FLC scattering is sometime comparable to
15 that of electrons on the nightside

Abstract

In the ring current dynamics, various loss mechanisms contribute to the ring current decay, including the loss to the upper atmosphere through particle precipitation. This study implements the field-line curvature (FLC) scattering mechanism in a kinetic ring current model and investigates its role in precipitating ions into the ionosphere. The newly included process is solved via a diffusion equation in the model with associated pitch-angle dependent diffusion coefficients. The simulation results indicate that (1) the FLC scattering process exerts mostly on energetic ions above 30 keV on the nightside where the magnetospheric configuration is more stretching. Such ion loss thereafter leads to a faster recovery of the ring current. (2) The FLC-associated ion precipitation mainly occurs in the outer region ($L > 5$ for protons and $L > 4.5$ for oxygen ions) on the nightside, and the oxygen ion precipitation takes place in a wider region than protons although its intensity is much lower. Comparisons with POES observations suggest that more precipitation is needed in the inner region, implying that other loss process is required in the model. (3) We further found that the precipitating energy flux of protons due to the FLC scattering can sometimes become comparable to the one from the electrons on the nightside, although electrons usually dominate the ionospheric energy deposit from the midnight eastward towards the dayside. (4) Finally, the FLC scattering process seems to be capable of explaining the formation of the isotropic boundary in the ionosphere.

1 Introduction

It is generally understood that the Earth ring current is composed of both electron and ion species, mainly H^+ , He^+ , and O^+ . The energy content of the ring current during storm time is dominantly from these ion species. Therefore ion loss processes can influence the intensity of the ring current while competing with energization processes. Ions can be supplied from the tail plasma sheet into the inner magnetosphere by convective electric field, gaining energies adiabatically. They move westward around the Earth due to magnetic gradient and curvature effects. Along their pathways, the ring current ions can be lost via charge exchange with neutral hydrogen when they encounter the geocorona [Dessler and Parker, 1959] and become neutralized. They can also lose energy and be scattered by the plasmaspheric ions and electrons due to Coulomb collision when they move through the ambient thermal plasma [Jordanova et al., 1996].

44 Of importance for the ring current decay are two additional collisionless scattering mechanisms,
 45 which may have significant impact on the ring current dynamics: wave-particle interactions and
 46 field line curvature (FLC) scattering. Electromagnetic ion cyclotron (EMIC) waves can resonate
 47 with energetic ring current ions once the wave frequency satisfies the resonate condition. While
 48 this process depends on the wave intensity and location, the FLC scattering is controlled by the
 49 geometry of magnetic field lines and occurs where the field line curvature radius is comparable
 50 to the gyroradius of particles [*Tsyganenko*, 1982; *Delcourt et al.*, 1996; *Sergeev et al.*, 1983], thus
 51 resulting in chaotic motion of the particles. Due to the much smaller gyroradius of electrons, the
 52 FLC scattering loss is more efficient on ions. Stretched magnetic field lines possess smaller curvature
 53 radius and therefore are more applicable for FLC scattering. Such condition often appears near
 54 the equatorial current sheet on the nightside, and FLC scattering is also named as current sheet
 55 scattering. Both collisionless mechanisms play the role of scattering ring current ions and changing
 56 particle distributions. *Ebihara et al.* [2011] examined the decay of ring current due to FLC scattering
 57 and found that the ring current shows rapid recovery with a e-folding time of 6 hour when the
 58 FLC scattering is included, as opposed to a e-folding time of 12 hour when it is excluded. Their
 59 study assumed that the FLC scattering works on protons only while its impact on other ion species
 60 was not considered. However it is known that the oxygen ions could sometime exceed the number
 61 density of protons and are of the same importance to the ring current growth during geomagnetic
 62 disturbed time [*Fernandes et al.*, 2017; *Yue et al.*, 2019] and that the oxygen ion is more effectively
 63 influenced by the FLC scattering because of its larger gyroradius, therefore the contribution of O^+
 64 precipitation may not be negligible. The study of *Ebihara et al.* [2011] thus provided a lower limit
 65 of the rapid decay of the ring current due to FLC scattering mechanism.

66 Besides the impact on the ring current dynamics, the FLC scattering process is believed to be
 67 associated with the formation of isotropic boundary (IB) [*Sergeev et al.*, 1993; *Sergeev and Gvozde-*
 68 *vsky*, 1995; *Meurant et al.*, 2007], a region in the auroral zone where the precipitating flux changes
 69 abruptly. Equatorward of the IB, the trapped particle flux is much higher than the precipitating
 70 flux, while the two are comparable poleward of the IB. In other words, the loss cones are filled up
 71 at higher latitudes whereas they are empty at lower latitudes of the IB. This boundary is identified
 72 in many observations as the low-Earth-orbit satellites (e.g., DMSP, NOAA/POES) travel across

73 it [*Newell et al.*, 1998; *Dubyagin et al.*, 2018]. Such a boundary characterizes a transition from
 74 weak precipitation to strong isotropic precipitation at higher latitudes and maps to the magneto-
 75 sphere location across which the rate of pitch angle scattering varies greatly. While EMIC waves
 76 are suggested to play a part, mostly at lower latitudes and local-time dependent, studies show that
 77 the FLC scattering may act as the major process for the IB formation [*Ganushkina et al.*, 2005;
 78 *Haiducek et al.*, 2018; *Yue et al.*, 2014; *Dubyagin et al.*, 2018].

79 Resulting from the ring current ion scattering loss, proton precipitation is produced into the
 80 upper atmosphere, which subsequently generates proton auroras. They are typically observed in
 81 two spatial regions [*Sraas et al.*, 1977], with one at high latitudes, corresponding to proton auroral
 82 oval, and the other one at subauroral region, separated from the high-latitude electron and proton
 83 auroral ovals. The latter often appears as spots or bands extended longitudinally. Previous studies
 84 have found close association between subauroral proton precipitation with EMIC waves in different
 85 locations (see review by [*Frey*, 2007; *Yahnin and Yahnina*, 2007]), such as dayside proton flashes
 86 [*Fuselier et al.*, 2004; *Hubert et al.*, 2003] and afternoon/nightside detached proton arcs [e.g., *Immel*
 87 *et al.*, 2002; *Spasojevic et al.*, 2004; *Spasojevic and Fuselier*, 2009; *Jordanova et al.*, 2007; *Nishimura*
 88 *et al.*, 2014]. The EMIC wave-driven proton precipitation could occur in localized regions where
 89 the local plasma conditions meet instability threshold and excite EMIC waves [e.g., *Jordanova*
 90 *et al.*, 1997]. Such locations can be spotty or elongated, as inferred from the auroral images. On
 91 the other hand, the FLC scattering-driven proton precipitation may take place over a much wider
 92 region if the nightside magnetic field lines are sufficiently stretched in a global scale. With the
 93 proton precipitation, one can monitor the degree of magnetic field stretching in the magnetotail
 94 and further help understand the magnetic mapping. *Liang et al.* [2013] proposed a technique
 95 to derive the magnetic field line curvature with in-situ measurements and evaluate the proton
 96 precipitation fluxes to estimate the MI mapping. Their study excluded the effects of EMIC waves
 97 on the precipitation by selecting events without EMIC activities. While it is highly possible that
 98 the proton precipitation led by EMIC-proton interactions and that due to FLC scattering coexists,
 99 the assessment on the role of both mechanisms is required in order to achieve better understanding
 100 of the proton auroral dynamics. However, compared to extensive studies on the association of
 101 proton aurora precipitation with EMIC waves [e.g., *Jordanova et al.*, 2007; *Nishimura et al.*, 2014;

102 *Yahnina and Yahnin, 2014; Yahnin and Yahnina, 2007; Spasojevic and Fuselier, 2009; Spasojevic*
 103 *et al., 2004; Fuselier et al., 2004; Chen et al., 2014*], the investigation on the association with the
 104 FLC scattering is still lacking.

105 Recently, *Chen et al. [2019]* included the FLC scattering mechanism in their RCM-E ring
 106 current model and compared the electron and ion precipitating flux and their respective effects on
 107 the ionospheric electrodynamics. They found that the FLC-associated ion scattering contributes
 108 much less to the precipitating energy flux and thus the resultant conductance of the ion diffuse
 109 aurora is far smaller than that of electron aurora. They used a simplified model for the FLC
 110 scattering loss rate, independent on pitch angles. In this study, we will also investigate the effect of
 111 FLC scattering on the ionospheric ion precipitation, as well as on the ring current decay. However,
 112 unlike *Chen et al. [2019]*, we implement the FLC scattering mechanism in the ring current model as a
 113 diffusion process by solving related diffusion coefficients that are energy and pitch angle dependent.
 114 We simulate the March 17, 2013 storm event to understand the role of FLC scattering in changing
 115 the ring current dynamics, the global pattern of diffuse aurora, and the IB positions. Section 2
 116 describes the model and the newly implemented FLC scattering loss mechanism. Section 3 presents
 117 simulation results on the morphology of ion precipitation associated with the FLC scattering, the
 118 subsequent effects on the ring current decay and ionospheric precipitation, as well as the relationship
 119 with the IB. Section 4 summarizes this study.

120 2 Model description

121 The kinetic ring current model used to study the role of FLC scattering is the ring current-
 122 atmosphere interactions model (RAM) coupled with a self-consistent (SC) magnetic field (B) and
 123 electric field code [*Jordanova et al., 2006; Zaharia et al., 2006; Yu et al., 2017*]. This RAM-SCB
 124 model mainly solves the bounce-averaged Fokker-Planck equation of distribution functions $F_l(t)$ for
 125 three ring current ion species (H^+ , He^+ , O^+) and electrons:

$$\begin{aligned} & \frac{\partial F_l(t, R, \phi, E, \alpha)}{\partial t} + \frac{1}{R_o^2} \frac{\partial}{\partial R_o} (R_o^2 \langle \frac{dR_o}{dt} \rangle F_l) + \frac{\partial}{\partial \phi} (\langle \frac{d\phi}{dt} \rangle F_l) \\ & + \frac{1}{\gamma p} \frac{\partial}{\partial E} (\gamma p \langle \frac{dE}{dt} \rangle F_l) + \frac{1}{h\mu_o} \frac{\partial}{\partial \mu_o} (h\mu_o \langle \frac{d\mu_o}{dt} \rangle F_l) \end{aligned}$$

$$= \langle \left(\frac{\partial F_l}{\partial t} \right)_{loss} \rangle \quad (1)$$

126 where the distribution function F_l is solved in the magnetic equatorial plane within a radial
 127 distance of $2.0 < R < 6.5 R_e$, covering all magnetic local times ϕ , pitch angles α ($\mu = \cos \alpha$, α from 0
 128 to 90°), and kinetic energy E from 0.15 to 400 keV. The subscription l represents particle species,
 129 the bracket $\langle \rangle$ denotes the bounce-average effect, the subscription o indicates the equatorial plane,
 130 p is the relativistic momentum of the particle, γ is the Lorentz factor, and h , which is proportional
 131 to the bounce period along magnetic field lines, is defined by:

$$h(\mu_o) = \frac{1}{2R_0} \int_{s_m}^{s'_m} \frac{ds}{\sqrt{(1 - B(s)/B_m)}} \quad (2)$$

132 Here, B_m is the magnetic field at the mirror point, ds is a distance interval along the field line, and
 133 R_0 is the distance between the Earth center and the intersection of the field line with the equatorial
 134 plane.

135 The time-dependent conditions that drive the variations of the above distribution function
 136 mainly lie in the following three aspects: (1) the outer boundary conditions at $6.5 R_e$, (2) the
 137 electric field condition, and (3) the magnetic field condition. The outer boundary condition, assumed
 138 isotropic, is obtained from the Los Alamos geosynchronous spacecraft that measure particle fluxes at
 139 various energy channels. The measured ion fluxes are decoupled into different ion species according
 140 to their statistical fractions derived by *Young et al.* [1982]. These fractions vary as a function of
 141 Kp index. The electric field or the electric potential is self-consistently estimated within the ring
 142 current model [*Yu et al.*, 2017]. Note that the inductive electric field is not included in this study.
 143 Mapped to the equatorial plane, the ionospheric electric potential is determined by field-aligned
 144 currents (FACs) and ionospheric conductance. The FACs, mainly Region-2 type, are diverted from
 145 the partial ring current [*Vasyliunas*, 1970] in the equator. The ionospheric conductance is originated
 146 from two energy sources: the solar radiation and electron precipitation. The solar radiation induced
 147 conductance can be estimated based on empirical functions with solar zenith angle and F10.7
 148 index [*Moen and Brekke*, 1993]. The electron precipitation associated conductance is determined
 149 by Robinson formula [*Robinson et al.*, 1987] that relates the conductance to the energy flux and

150 averaged energy of precipitating electrons that are diffused into loss cone from the ring current.
 151 As for the magnetic field condition, the ring current model is coupled self-consistently to a 3-D
 152 equilibrium code that computes the magnetic field from the anisotropic plasma conditions [*Zaharia*
 153 *et al.*, 2004, 2006]. With the supply of plasma source from the boundary, mostly on the nightside,
 154 the above electric and magnetic field drive the particles to move toward and around the Earth,
 155 violating the third adiabatic invariant if the global change of the magnetic field configuration is
 156 on the order of drift period of particles, thus leading to their energization and the increase of ring
 157 current intensity.

158 The loss processes that decay the ring current stem from both ions and electrons. Although
 159 electrons contribution is minor to the ring current energy content as opposed to ions, it is found
 160 to be not negligible as electrons could contribute as much as 20% in storms [*Jordanova et al.*,
 161 2012]. In addition to being depleted at the dayside magnetopause boundary, the loss of electrons
 162 are partly caused by scattering into their loss cones and precipitating into the upper atmosphere.
 163 Such scattering process is mostly a result of cyclotron wave-particle interactions when the electrons
 164 gyrorate at a frequency Ω_c that satisfies the resonant condition. Gyroresonant interactions with
 165 waves can lead particles to diffuse in pitch angle. The responsible waves included in this ring current
 166 model are whistler-mode waves, such as chorus waves outside plasmopause and hiss waves inside
 167 plasmopause [e.g., *Ni et al.*, 2016]. In this study, the electrostatic electron cyclotron harmonic
 168 (ECH) wave is not included.

169 The electron scattering process, or diffusion, can be accounted for via the diffusion equation:

$$\begin{aligned} \langle \left(\frac{\partial F_l}{\partial t} \right) \rangle = & \frac{1}{h\mu_o} \frac{\partial}{\partial \mu_o} \left[h\mu_o \langle D_{\mu_o\mu_o} \rangle \frac{\partial F_l}{\partial \mu_o} \right] \\ & \langle D_{\mu_o\mu_o} \rangle = (1 - \mu_o^2) \langle D_{\alpha\alpha} \rangle \end{aligned} \quad (3)$$

170 where $\langle D_{\alpha\alpha} \rangle (E, \alpha)$ is bounce-averaged pitch angle diffusion coefficients associated with wave-
 171 particle resonant interactions. The coefficients associated with chorus waves are determined from
 172 quasi-linear theory using the PADIE code [*Glauert and Horne*, 2005; *Horne et al.*, 2013; *Glauert*
 173 *et al.*, 2014], based on statistical observations of wave properties for regions outside the plasmopause.
 174 The coefficients associated with hiss waves are computed from a similar code by *Albert* [2005]. The

175 electrons diffused into their loss cones then participate in changing the auroral conductance, as a
 176 major energy source to the ionosphere.

177 For ions, their loss processes in the model include charge exchange with geocoronal hydrogens,
 178 drift out of the magnetopause boundary, atmospheric collisional loss, and collisionless pitch angle
 179 diffusion into loss cones for precipitation. The collisionless scattering mechanism newly implemented
 180 in the model is the FLC scattering, which is solved via the same diffusion equation in Eqn. (3). The
 181 diffusion coefficients $D_{\alpha\alpha}$ are computed based on the geometry of magnetic field lines, previously
 182 formulated by *Young et al.* [2008]:

$$\begin{aligned}
 D_{\alpha\alpha} &= D \frac{N^2 \sin^2(\omega(\varepsilon)\alpha_0) \cos^{2b(\varepsilon)}(\alpha_0)}{\sin^2(\alpha_0) \cos^2(\alpha_0)} \\
 D &= \frac{A_{max}^2(\varepsilon, \eta_1, \eta_2)}{2\tau_B} \\
 N &= [\sin(\omega(\varepsilon)\alpha_0) \cos^{b(\varepsilon)}(\alpha_0)]^{-1} |_{\alpha_0=\bar{\alpha}_0} \\
 A_{max} &= \exp(c(\varepsilon))(\eta_1^{a1(\varepsilon)} \eta_2^{a2(\varepsilon)} + d(\varepsilon))
 \end{aligned} \tag{4}$$

183 Here $\varepsilon = R_G/R_C$ is a parameter representing the degree of chaotic scattering due to FLC effects.
 184 R_G is the particle gyroradius in the equatorial plane, and R_C is the field line curvature radius:

$$\frac{1}{R_c} = (\vec{b} \cdot \nabla) \vec{b} \tag{5}$$

185 where \vec{b} is the unit vector of magnetic field at the magnetic equator $\vec{b} = \vec{B}/B$. The critical
 186 threshold of ε is chosen at 0.1 in this study, below which the chaotic scattering is considered weak
 187 and the diffusion coefficient is not calculated. This is equivalent to the theoretical adiabaticity
 188 parameter K , the reversal of ε . Typically, a value of $K = 8$ marks the transition from a weakly
 189 scattering condition to a strongly scattering condition ([*Serggev et al.*, 1983]) and is applied in many
 190 studies for studying the IB location. [e.g., *Liang et al.*, 2013; *Yue et al.*, 2014; *Gilson et al.*, 2012].
 191 But this theoretical value has recently been challenged because researchers found that this scattering
 192 threshold could be much higher or within a certain range [*Ilie et al.*, 2015; *Dubyagin et al.*, 2018;
 193 *Haiducek et al.*, 2018]. Recent study of *Haiducek et al.* [2018] used multiple magnetospheric models
 194 to determine the accuracy of K estimation and reported constraints on the range of K values, which

195 subsequently is found to be close to the above theoretical threshold. *Dubyagin et al.* [2018] also
 196 reported statistical distribution of the estimated K parameter to be around 9-13. Therefore, in this
 197 study, we adopt the ε value of 0.1 as the transition threshold, close to the reversal of $K = 10$.

198 In the above equation, $\eta_1 = R_C(\delta^2 R_C / \delta s^2)$ and $\eta_2 = R_C^2 / B_0(\delta^2 B_0 / \delta s^2)$ are measures of the
 199 changing curvature radius R_C and magnetic field B_0 in the equatorial plane, respectively (s is the
 200 distance along the field line away from the equator). τ_B is the bounce period between two magnetic
 201 mirror points, equivalent with the h parameter in Eqn. (2). $\bar{\alpha}_0$ is the equatorial pitch angle, at
 202 which the angle-dependent quantity $\sin(\omega\alpha_0) \cos^b(\varepsilon)(\alpha_0)$ reaches its maximum. [*Young et al.*, 2002].
 203 Parameters of $a1(\varepsilon)$, $a2(\varepsilon)$, $c(\varepsilon)$, and $d(\varepsilon)$ are determined in the form of $q = \sum_{n=0}^N q_n \varepsilon^{-n}$ with the
 204 coefficients q_n listed in Table 2 of *Young et al.* [2002].

205 From the above formula, it is evident that $D_{\alpha\alpha}$ is controlled by the parameter of ε , which
 206 depends on not only the geometry of the in-situ magnetic field lines, but also the gyroradius, or the
 207 mass of particles. So as the ring current electrons have much smaller gyroradius than the curvature
 208 radius, the electrons are unlikely to be influenced by the FLC scattering process. On the other hand,
 209 ring current ions (H^+ , He^+ , O^+) with comparable gyroradius can experience scattering. Among
 210 the three species, the O^+ has the largest gyroradius, so it would experience the FLC scattering
 211 most easily. In this study, we only consider the FLC effect on the ion scattering.

212 3 Simulation results

213 In order to understand the role of FLC scattering mechanism in ion precipitation and the decay
 214 of ring current intensity, we perform two simulations with the FLC scattering process included and
 215 excluded, respectively. The storm event is chosen at March 17, 2013, a CME-driven event with its
 216 minimum Dst approaching -140 nT. Figure 1 shows the solar wind, interplanetary, and geomagnetic
 217 conditions. The largely increased solar wind speed, solar wind density, and southward turning of
 218 the IMF Bz component lead to the enhancement of Dst and AE index, corresponding to the sudden
 219 storm commencement (SSC). For the rest of the day, substantial substorm injections continue and
 220 the Dst index decreases to -100 nT around 10:30 UT and further drops to around -140 nT at 20:00
 221 UT, after which the recovery phase begins.

3.1 Morphology of ion precipitation associated with FLC scattering

Figure 2 shows the global distribution of the rigidity parameter ε and the corresponding pitch angle diffusion coefficients $D_{\alpha\alpha}$ for different ion species at $E=50$ keV and $\alpha=50^\circ$. All these plots are chosen at the time of the first Dst minimum (i.e., 10:30 UT). The ε value for all ion species is generally larger on the nightside than on the dayside, a result of that the nightside magnetic field lines are more stretched with smaller field line curvature. As the O^+ ion has the largest gyroradius among the three, its ε is the greatest, and it would experience the FLC scattering on the dayside the most easily since it meets the criterion of $\varepsilon > 0.1$ in a wider region than He^+ , and even much wider than H^+ . As expected, the pitch angle diffusion coefficient $D_{\alpha\alpha}$ above the FLC scattering threshold, i.e., the non-blank area in the plot (middle column), shows wider coverage over the globe, although the magnitude is not necessarily the largest. Figure 2 (right column) shows that in general, for individual ion species, the $D_{\alpha\alpha}$ is larger at higher energies, and reaches the highest around the pitch angle of 50° , suggesting that the FLC mechanism can more effectively scatter ions with higher energies and intermediate pitch angles. Among the three ions, the diffusion coefficient for the H^+ appears to be the largest for higher energies ($E > 10$ keV), but it is smaller at lower energies ($E < 10$ keV). The coefficient of O^+ is larger at lower energies. Such a reversed order in the $D_{\alpha\alpha}$ indicates that for ions at a particular kinetic energy E and pitch angle, the scattering efficiency is larger for O^+ ions when E is small, but it is larger for H^+ ions when E is larger.

Figure 3 compares the total precipitating flux within the ion loss cone at different energies from two simulations at 10:30 UT. The results without FLC scattering loss show that precipitation mostly occurs on the dusk-to-nightside sector outside L of 3.5. Ions with lower energies are precipitated more. The H^+ ions show the largest precipitating flux among the three species and He^+ ions precipitate the least. Such precipitation is a result of magnetospheric convection; as the particles are transported earthward and the loss cone widens, particles with small pitch angles precipitate [Jordanova *et al.*, 1996]. Regardless of the ion species and the intensity of the flux, the global morphology of the precipitation is the same for these ions. That is, the precipitation occurs in the same MLT region outside the plasmapause for the same energy.

249 As the FLC scattering is included in the simulation, the precipitation on the nightside increases
 250 significantly. Among the three ion species, the H^+ and He^+ precipitation mostly takes place in
 251 the outer region ($L > 5$) in the nightside sector, while the O^+ precipitation zone extends into the
 252 afternoon and morning sectors, in addition to the nightside region. Its radial coverage is also much
 253 larger on the nightside. Ions with higher energies tend to precipitate slightly in the inner region
 254 and more into the dayside sector. In contrary to the H^+ precipitation, the O^+ precipitation at $E =$
 255 50 keV shows asymmetry in the global pattern. The precipitation is much less on the dawn-to-noon
 256 sector than the other area, possibly an indication on the drift path of source population as they
 257 move around the Earth.

258 From the global distribution of proton precipitation with the FLC scattering included, we can
 259 easily identify the sharp earthward boundary of the precipitation for these ions, which may be
 260 related to the isotropy boundary. It is evident that the precipitation boundary is not only energy
 261 and MLT dependent but also ion species dependent. For example, the boundary of $E = 50$ keV H^+
 262 is around $L = 5$ at the midnight and moves outwards to $L = 6$ on the dawnside/duskside. In
 263 other words, the ionospheric latitude for the precipitation boundary is at the lowest latitudes on
 264 the midnight and shifts to higher latitudes while moving eastward or westward. Such boundary is
 265 further earthward at higher energies. In contrast, the precipitating boundary of O^+ is even closer
 266 to the Earth than the light ions. These tendencies were also reported in previous studies [e.g., *Yue*
 267 *et al.*, 2014] that estimated the isotropy boundary based on the criterion of $K = 8$ (or $\varepsilon = 0.125$).
 268 Thus, the FLC scattering may be associated with the formation of isotropy boundary, as will be
 269 discussed below.

270 **3.2 Contribution of FLC scattering to the ring current decay and ionospheric** 271 **precipitation**

272 As shown above, the FLC scattering brings about substantial ion precipitation compared to
 273 the adiabatic loss by magnetospheric convection, meaning that the ring current loses a large amount
 274 of ion population. Figure 4 shows the simulated Dst index compared to the observed SYM-H index.
 275 The simulation uses Dessler-Parker-Sckopke (DPS) relationship [*Dessler and Parker*, 1959; *Sckopke*,
 276 1966] to estimate the energy content of the ring current and then determine the associated Dst index.

277 The ring current between 06:00 and 10:00 UT drops rapidly in both simulations, suggesting that the
 278 energization process dominates over the loss processes in the storm main phase. On the other hand,
 279 the ring current is remarkably weaker in the recovery phase when the FLC effect is considered and
 280 recovers slightly faster than the case without the FLC scattering. The difference between the two
 281 Dst indices is about 15 nT, a factor of 20%, implying that the FLC scattering of ions additionally
 282 removes about 20% of the ion population from the ring current populations. It should be noted that
 283 the ring current model only simulates the ring current while the observed SYM-H index represents
 284 the contribution from all types of current systems, including the magnetopause current and tail
 285 currents, which are absent in the model. This is probably the reason that the overall Dst index in
 286 the simulation is not as strong as in the observation.

287 We further compare the precipitation with in-situ measurements from low-earth orbit (LEO)
 288 NOAA/POES satellites. With several identical spacecraft flying along different meridians, global
 289 coverage of precipitation is obtained. Figure 5 (a) shows observed proton precipitation of $30 < E < 80$
 290 keV at four MLT sectors. The data is binned every 0.5 hour with a radial resolution of $0.25 R_e$. The
 291 proton precipitation on the dusk-to-night sector ($15 < \text{MLT} < 3$) is profound during the storm main
 292 phase as well as in the prolong recovery phase. In the storm main phase from 06:00 to 10:30 UT,
 293 the inner region with $3.5 < L < 5$ is gradually filled up with loss cone protons. In the recovery phase,
 294 the earthward inner boundary of precipitation slightly migrates outwards with the precipitation
 295 intensity decreased. In the sector of $15 < \text{MLT} < 21$, the outer region ($L > 5$) shows nearly lack of
 296 precipitation after 18:00 UT, while the inner region still possesses strong precipitating flux. On the
 297 morning and dayside ($3 < \text{MLT} < 15$), the precipitation mostly occurs outside $L=4.5$, and is much
 298 weaker in both the storm main phase and recovery phase.

299 In the simulation without FLC scattering, the proton precipitation (30-80 keV) in the dusk-
 300 to-night sector ($15 < \text{MLT} < 3$) appears within a large region outside $L=3$ in the storm main phase
 301 and recovery phase, similar to the distribution in observations. However, the magnitude is notably
 302 smaller, suggesting that the loss of protons from magnetospheric convection at $30 < E < 80$ keV in the
 303 model cannot account for the observed precipitation. When the FLC scattering loss is introduced, it
 304 is found that the proton precipitation in the outer zone ($L > 5.5$) is largely enhanced, which therefore

305 agrees better with the observation qualitatively. In the midnight sector ($21 < \text{MLT} < 3$), the intensity
 306 appears larger than the data in the same zone. In the dusk sector ($15 < \text{MLT} < 21$), the outer zone
 307 precipitation is weaker and remarkably drops after 18:00 UT, which is consistent with the data.
 308 However, across all the MLTs, the inner region ($3.5 < L < 5$) still lacks sufficient precipitation, which
 309 may be attributed to the missing of other necessary collisionless loss mechanisms, such as EMIC
 310 waves.

311 Similarly, with the FLC scattering loss included, the O^+ precipitation is significantly enhanced
 312 in the outer zone ($L > 4.5$ on the nightside, and $L > 5$ on the dayside), as opposed to the case without
 313 FLC scattering loss, in which only weak precipitation occurs in the dusk and night sectors and it is
 314 completely empty on the dayside. The O^+ precipitation appears across a wider L region than the
 315 proton precipitation, although the precipitation intensity for $30 < E < 80$ keV is not as large. It further
 316 shows larger flux on the dayside ($9 < \text{MLT} < 15$) that is missing in the proton precipitation (Since no
 317 O^+ precipitation is available from the POES satellite, comparisons are not made available).

318 **3.3 Energy source to the ionosphere due to ion precipitation**

319 We further investigate the contribution of the ion precipitation to the ionospheric energy deposit
 320 by comparing with the electron precipitation. It is widely believed that the electron precipitation
 321 contains the dominant energy source into the upper atmosphere and the contribution of ions is
 322 usually omitted. With the FLC scattering process included, we compare the consequent contribution
 323 from all ion species. Figure 6 shows the spatial distribution of precipitating energy flux of electrons,
 324 protons, helium ions, and oxygen ions at 10:30 UT. The precipitating energy flux is computed
 325 by integrating the differential flux within the loss cone over $150 \text{ eV} < E < 400 \text{ keV}$. The electron
 326 precipitation clearly dominates the energy budget from the post-midnight eastward to the dayside.
 327 On the nightside, large electron precipitation extends to latitudes as low as 51° and the energy
 328 deposit almost reaches $10 \text{ ergs/cm}^2/\text{s}$ at $\text{MLT}=9$ and $\text{MLat} = 60^\circ$. In contrast, the ion precipitation
 329 is mostly centered around the midnight and decreases towards dayside. The proton energy flux is
 330 the largest among the three ion populations, followed by the oxygen and helium ions. It is noted
 331 that on the nightside ($21 < \text{MLT} < 3$), the proton energy flux appears to be close to that of electrons

332 at mid-latitudes, suggesting that the proton precipitation also carries considerable energy source
 333 down to the upper atmosphere on the nightside.

334 Figure 7 shows the temporal evolution of precipitating energy flux at midnight (MLT=24).
 335 The energy flux of each species is significantly enhanced after 06:00 UT as the storm begins and
 336 the nightside magnetic field stretches. While increased electron precipitating energy flux frequently
 337 penetrates to lower latitudes, possibly by enhanced wave-particle interactions as tail plasma are
 338 injected earthward, the ions mostly contribute to latitudes above 55° , where the magnetosphere
 339 undergoes large stretching. The intensity of the energy flux due to proton precipitation is close to
 340 that of electrons throughout the storm main phase, indicating that on the nightside, ion precipitation
 341 owing to the FLC scattering also produces remarkable energy source to the ionosphere, which may
 342 further enhance the ionization in the upper atmosphere and local conductivity. In our next study,
 343 we will incorporate this additional energy source in the calculation of the ionospheric conductance.
 344 Again, the oxygen ions provide a larger coverage of precipitation source energy, but at a secondary
 345 level in its intensity as compared to protons.

346 **3.4 Relationship with the isotropy boundary**

347 Finally, whether the FLC scattering is associated with the formation of isotropic boundary
 348 is examined. We follow the methods in *Dubyagin et al.* [2018] to identify the IB location from
 349 NOAA satellite observations of 30-80 keV proton fluxes. Two NOAA satellites (MetOP-02 and
 350 NOAA-19) travel through the auroral zone in the pre-midnight and post-midnight sector respectively
 351 during the storm event, and thus provide a good opportunity to compare with simulation results
 352 because the FLC scattering process is predominantly effective on the nightside. As demonstrated
 353 in Figure 8 (a, b), across the boundary towards lower latitudes (or lower L shells), the precipitating
 354 (from 0° telescope) proton flux is lower than the trapped (from 90° telescope) proton flux and
 355 deviates more and more as moving towards equatorward (lower L shells). The two are however
 356 in comparable magnitude at higher latitudes (larger L shells) of the boundary (i.e., a signature of
 357 isotropic distribution). In case of encountering two boundaries (high-latitude and low-latitude IBs)
 358 [*Dubyagin et al.*, 2018], we choose the high-latitude boundary because the low-latitude boundary
 359 may be attributed to local dynamics such as EMIC waves.

360 Figure 8 (c) shows IB locations (solid lines) obtained from the two satellites. During the entire
 361 storm event, although their orbits slightly shift in local times, the variation is small within 1-2
 362 local hours. From the simulation results, we obtain the boundary along the satellite trajectory by
 363 selecting the position where the rigidity parameter of $\varepsilon = 0.1$ for protons of 50 keV, a criterion used
 364 in many previous studies [e.g. *Serggeev et al.*, 1983; *Ganushkina et al.*, 2005; *Yue et al.*, 2014]. It is
 365 found that in storm time, the boundary determined from the model results move to lower L shells,
 366 consistent with the trends in the data, although at pre-storm time, the model shows a much more
 367 earthward location than the data. During the storm time (after 09:00 UT), the model's boundary
 368 is around 4.5, while the observations show that IB locations generally fluctuate between L=3.5 and
 369 L=4.5, slightly closer to the Earth than the model results. Hence, the modeled isotropic boundary
 370 is at larger L-shells than observations by about 20%, indicating that the stretching of the nightside
 371 magnetic field lines and subsequent FLC scattering is roughly responsible for the formation of sharp
 372 IB boundaries.

373 4 Summary

374 In this study, we implement an additional collisionless loss mechanism in the ring current
 375 model: field line curvature (FLC) scattering, and investigate its effects on the ring current decay
 376 and contribution to the ionospheric energy source and auroral isotropic boundary. The FLC scat-
 377 tering mechanism is solved via a diffusion equation with associated pitch angle diffusion coefficients.
 378 Ions with comparable gyroradius to the field line curvature radius undergo scattering and further
 379 precipitate down to the ionosphere when they are in the loss cones. The results are summarized as
 380 follows.

- 381 1. The FLC scattering mechanism can effectively diffuse ring current ions on the nightside where
 382 the magnetic field lines are more stretched. Compared to the protons, the heavy oxygen ions
 383 experience the scattering over a wider region due to its larger gyroradius. The precipitation
 384 of protons takes place mainly on the nightside outside L=5, while the oxygen ions precipitate
 385 outside L=4 and even on the dayside. With the FLC scattering included, the ring current
 386 energy content decreases and recovers sooner.

- 387 2. The comparisons with NOAA/POES 30-80 keV proton precipitating flux demonstrate that the
388 FLC scattering could account for the precipitation in the outer zone ($L > 5$) on the nightside.
389 But more precipitating flux is needed in the inner zone down to $L = 3.5$. Such additional
390 scattering process can be due to the EMIC waves, which is being investigated in an ongoing
391 project in our team.
- 392 3. The precipitating proton energy flux can at times be comparable to that of electrons at
393 midnight, suggesting that the ion precipitation also contributes significantly to the ionospheric
394 energy deposit and cannot be neglected. The oxygen ion precipitation, although at a smaller
395 intensity, occurs with a larger coverage at mid-latitudes. These additional energy source into
396 the ionosphere will be considered in our next study for a more comprehensive calculation of
397 ionospheric conductance.
- 398 4. The isotropic boundary, determined from NOAA satellites that travel across the pre-midnight
399 and post-midnight sectors, is compared to the FLC-associated boundary (i.e., $\varepsilon = 0.1$, below
400 which no scattering takes places and isotropic precipitation sharply drops). General agreement
401 of the two locations is achieved, although a small discrepancy of about 20% exists. The model's
402 boundary where isotropic precipitation sharply drops during storm time is around $L = 4.5$, while
403 the observations show the isotropic boundary between 3.5-4.5. We can therefore conclude that
404 the FLC scattering process could explain the formation of isotropic boundary to a large extent.

405 Acknowledgments

406 The authors thank the OMNIweb from NASA Goddard Space Flight Center for providing the
407 solar wind/interplanetary data and the Kyoto, Japan World Data Center System for providing
408 the SYM-H index and AE-index. The authors are also grateful to NOAA website for providing
409 POES data (<http://satdat.ngdc.noaa.gov/sem/poes/>). The RAM-SCB model code is available at
410 <https://github.com/lanl/RAM-SCB>.

411 The simulation data is available at <https://doi.org/10.5281/zenodo.3631152> [Yu *et al.*, 2020]. Simu-
412 lations were performed on TianHe-2 at National Supercomputer Center in Guangzhou, China. The
413 work at Beihang University was supported by the NSFC grants 41574156, 41821003, and 41974192.

414 The work at Los Alamos was conducted under the auspices of the U. S. Department of Energy, with
415 partial support from the National Aeronautics and Space Administration.

416 **References**

- 417 Albert, J. M. (2005), Evaluation of quasi-linear diffusion coefficients for whistler mode waves in a
418 plasma with arbitrary density ratio, *Journal of Geophysical Research: Space Physics*, *110*(A3),
419 doi:10.1029/2004JA010844, a03218.
- 420 Chen, L., V. K. Jordanova, M. Spasojevic, R. M. Thorne, and R. B. Horne (2014), Electromagnetic
421 ion cyclotron wave modeling during the geospace environment modeling challenge event, *Journal*
422 *of Geophysical Research Space Physics*, *119*(4), 2963–2977.
- 423 Chen, M. W., C. L. Lemon, J. Hecht, S. Sazykin, R. A. Wolf, A. Boyd, and P. Valek (2019),
424 Diffuse auroral electron and ion precipitation effects on rcm-e comparisons with satellite data
425 during the 17 march 2013 storm, *Journal of Geophysical Research: Space Physics*, *0*(0), doi:
426 10.1029/2019JA026545.
- 427 Delcourt, D. C., J. A. Sauvaud, R. F. M. Jr, and T. E. Moore (1996), On the nonadiabatic precipi-
428 tation of ions from the near-earth plasma sheet, *Journal of Geophysical Research Space Physics*,
429 *101*(A8), 17,409–17,418.
- 430 Dessler, A. J., and E. N. Parker (1959), Hydromagnetic Theory of Geomagnetic Storms, *J. Geophys.*
431 *Res.*, *64*, 2239–2252, doi:10.1029/JZ064i012p02239.
- 432 Dubyagin, S., N. Y. Ganushkina, and V. Sergeev (2018), Formation of 30keV proton isotropic
433 boundaries during geomagnetic storms, *Journal of Geophysical Research: Space Physics*, *123*(5),
434 3436–3459, doi:10.1002/2017JA024587.
- 435 Ebihara, Y., M.-C. Fok, T. J. Immel, and P. C. Brandt (2011), Rapid decay of storm time ring
436 current due to pitch angle scattering in curved field line, *Journal of Geophysical Research: Space*
437 *Physics*, *116*(A3), doi:10.1029/2010JA016000.
- 438 Fernandes, P. A., B. A. Larsen, M. F. Thomsen, R. M. Skoug, G. D. Reeves, M. H. Denton, R. H. W.
439 Friedel, H. O. Funsten, J. Goldstein, M. G. Henderson, J.-M. Jahn, E. A. MacDonald, and D. K.
440 Olson (2017), The plasma environment inside geostationary orbit: A van allen probes hope survey,
441 *Journal of Geophysical Research: Space Physics*, *122*(9), 9207–9227, doi:10.1002/2017JA024160.

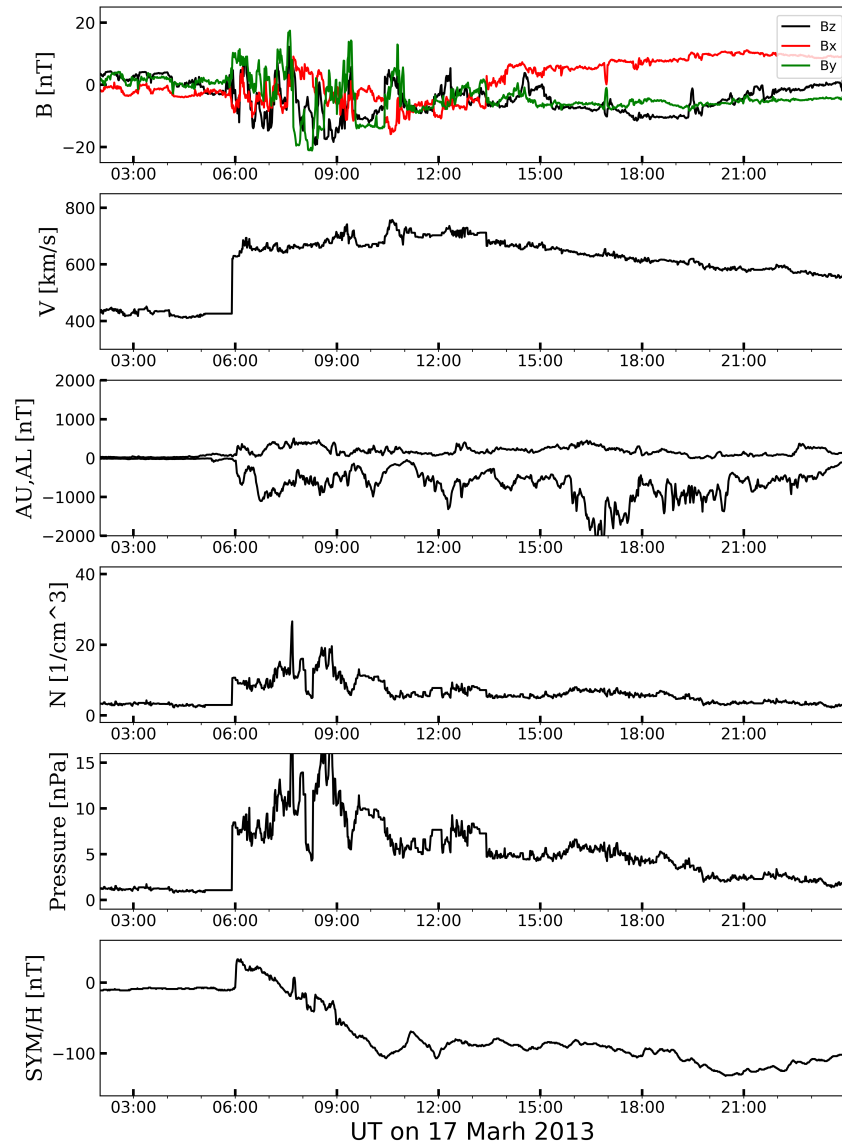
- 442 Frey, H. U. (2007), Localized aurora beyond the auroral oval, *Reviews of Geophysics*, *45*(1).
- 443 Fuselier, S. A., S. P. Gary, M. F. Thomsen, E. S. Claffin, B. Hubert, B. R. Sandel, and T. Immel
444 (2004), Generation of transient dayside subauroral proton precipitation, *Journal of Geophysical
445 Research: Space Physics*, *109*(A12), doi:10.1029/2004JA010393.
- 446 Ganushkina, N. Y., T. I. Pulkkinen, M. V. Kubyshkina, V. A. Sergeev, E. A. Lvova, T. A. Yahnina,
447 A. G. Yahnin, and T. Fritz (2005), Proton isotropy boundaries as measured on mid- and low-
448 altitude satellites, *Annales Geophysicae*, *23*(5), 1839–1847, doi:10.5194/angeo-23-1839-2005.
- 449 Gilson, M. L., J. Raeder, E. Donovan, Y. S. Ge, and L. Kepko (2012), Global simulation of proton
450 precipitation due to field line curvature during substorms, *Journal of Geophysical Research: Space
451 Physics*, *117*(A5), doi:10.1029/2012JA017562.
- 452 Glauert, S. A., and R. B. Horne (2005), Calculation of pitch angle and energy diffusion coeffi-
453 cients with the PADIE code, *Journal of Geophysical Research (Space Physics)*, *110*, A04206,
454 doi:10.1029/2004JA010851.
- 455 Glauert, S. A., R. B. Horne, and N. P. Meredith (2014), Three-dimensional electron radiation
456 belt simulations using the BAS Radiation Belt Model with new diffusion models for chorus,
457 plasmaspheric hiss, and lightning-generated whistlers, *Journal of Geophysical Research (Space
458 Physics)*, *119*, 268–289, doi:10.1002/2013JA019281.
- 459 Haiducek, J. D., N. Y. Ganushkina, S. Dubyagin, and D. T. Welling (2018), On the accuracy of adi-
460 abaticity parameter estimations using magnetospheric models, *Journal of Geophysical Research:
461 Space Physics*, *124*(3), 1785–1805, doi:10.1029/2018JA025916.
- 462 Horne, R. B., T. Kersten, S. A. Glauert, N. P. Meredith, D. Boscher, A. Sicard-Piet, R. M. Thorne,
463 and W. Li (2013), A new diffusion matrix for whistler mode chorus waves, *Journal of Geophysical
464 Research (Space Physics)*, *118*, 6302–6318, doi:10.1002/jgra.50594.
- 465 Hubert, B., J. C. Grard, S. A. Fuselier, and S. B. Mende (2003), Observation of dayside subauroral
466 proton flashes with image-fuv., *Geophysical Research Letters*, *30*(3), 263–263.
- 467 Ilie, R., N. Ganushkina, G. Toth, S. Dubyagin, and M. W. Liemohn (2015), Testing the magnetotail
468 configuration based on observations of low-altitude isotropic boundaries during quiet times, *Jour-
469 nal of Geophysical Research: Space Physics*, *120*(12), 10,557–10,573, doi:10.1002/2015JA021858.

- 470 Immel, T. J., S. B. Mende, H. U. Frey, L. M. Peticolas, C. W. Carlson, J. C. Gerard, B. Hubert,
471 and S. A. Fuselier (2002), Precipitation of auroral protons in detached arcs, *Geophysical Research*
472 *Letters*, *29*(11), 14–114–4.
- 473 Jordanova, V. K., L. M. Kistler, J. U. Kozyra, G. V. Khazanov, and A. F. Nagy (1996), Collisional
474 losses of ring current ions, *Journal of Geophysical Research Space Physics*, *101*(A1), 111.
- 475 Jordanova, V. K., J. U. Kozyra, A. F. Nagy, and G. V. Khazanov (1997), Kinetic model of the ring
476 current-atmosphere interactions, *Journal of Geophysical Research (Space Physics)*, *102*, 14,279–
477 14,292, doi:10.1029/96JA03699.
- 478 Jordanova, V. K., Y. S. Miyoshi, S. Zaharia, M. F. Thomsen, G. D. Reeves, D. S. Evans,
479 C. G. Mouikis, and J. F. Fennell (2006), Kinetic simulations of ring current evolution during
480 the Geospace Environment Modeling challenge events, *Journal of Geophysical Research (Space*
481 *Physics)*, *111*, A11S10, doi:10.1029/2006JA011644.
- 482 Jordanova, V. K., M. Spasojevic, and M. F. Thomsen (2007), Modeling the electromagnetic ion
483 cyclotron wave-induced formation of detached subauroral proton arcs, *Journal of Geophysical*
484 *Research: Space Physics*, *112*(A8), doi:10.1029/2006JA012215.
- 485 Jordanova, V. K., D. T. Welling, S. G. Zaharia, L. Chen, and R. M. Thorne (2012), Modeling ring
486 current ion and electron dynamics and plasma instabilities during a high-speed stream driven
487 storm, *Journal of Geophysical Research (Space Physics)*, *117*(A9), doi:10.1029/2011JA017433.
- 488 Liang, J., E. Donovan, E. Spanswick, and V. Angelopoulos (2013), Multiprobe estimation of field
489 line curvature radius in the equatorial magnetosphere and the use of proton precipitations in
490 magnetosphere-ionosphere mapping, *Journal of Geophysical Research: Space Physics*, *118*(8),
491 4924–4945, doi:10.1002/jgra.50454.
- 492 Meurant, M., J.-C. Grard, C. Blockx, E. Spanswick, E. F. Donovan, B. Hubert, V. Coumans, and
493 M. Connors (2007), El - a possible indicator to monitor the magnetic field stretching at global
494 scale during substorm expansive phase: Statistical study, *Journal of Geophysical Research: Space*
495 *Physics*, *112*(A5), doi:10.1029/2006JA012126.
- 496 Moen, J., and A. Brekke (1993), The solar flux influence on quiet time conductances in the auroral
497 ionosphere, *grl*, *20*, 971–974, doi:10.1029/92GL02109.

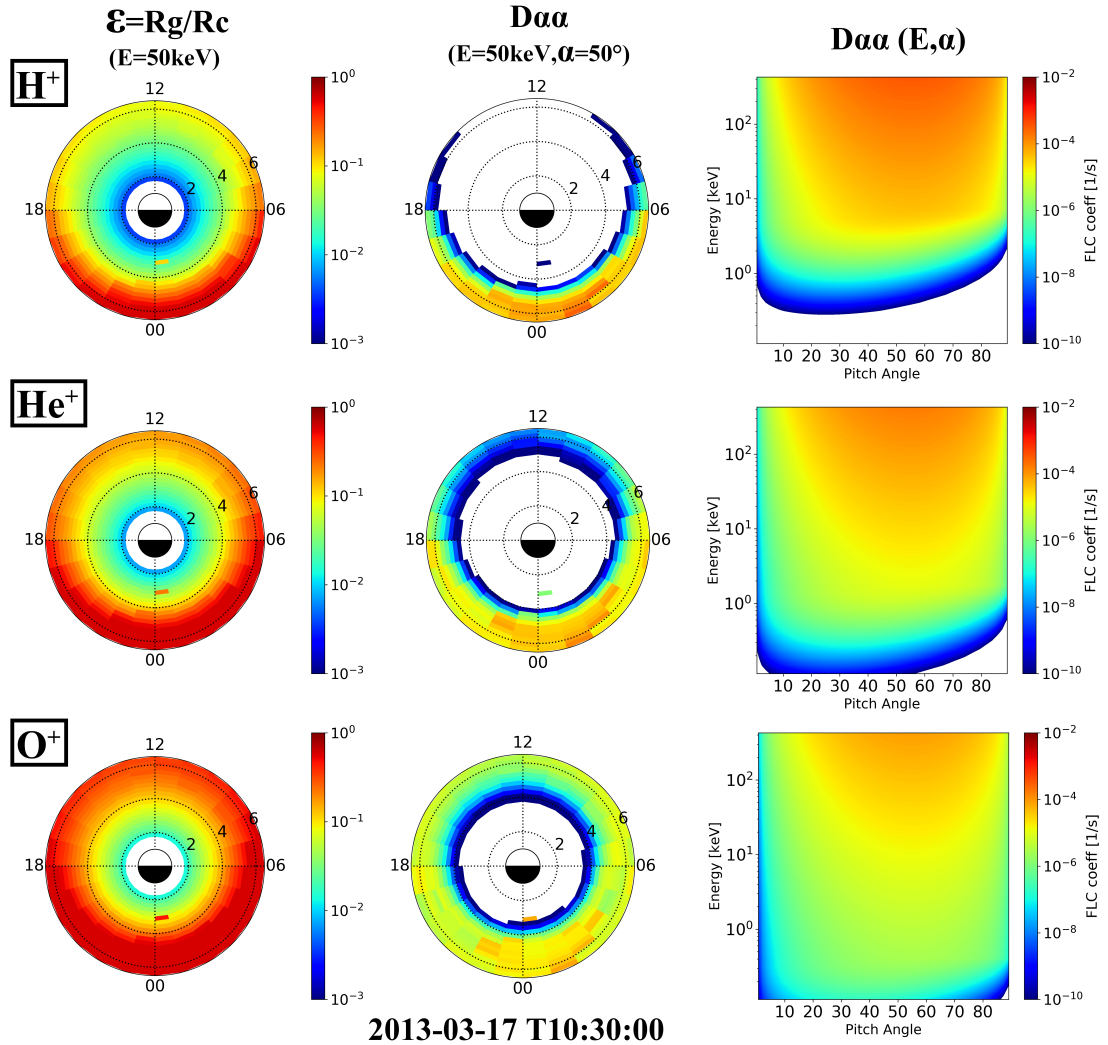
- 498 Newell, P. T., V. A. Sergeev, G. R. Bikkuzina, and S. Wing (1998), Characterizing the state
499 of the magnetosphere: Testing the ion precipitation maxima latitude (b2i) and the ion
500 isotropy boundary, *Journal of Geophysical Research: Space Physics*, *103*(A3), 4739–4745, doi:
501 10.1029/97JA03622.
- 502 Ni, B., R. M. Thorne, X. Zhang, J. Bortnik, Z. Pu, L. Xie, Z.-j. Hu, D. Han, R. Shi, C. Zhou, and
503 X. Gu (2016), Origins of the earth’s diffuse auroral precipitation, *Space Science Reviews*, *200*(1),
504 205–259, doi:10.1007/s11214-016-0234-7.
- 505 Nishimura, Y., J. Bortnik, W. Li, L. R. Lyons, E. F. Donovan, V. Angelopoulos, and S. B. Mende
506 (2014), Evolution of nightside subauroral proton aurora caused by transient plasma sheet flows,
507 *Journal of Geophysical Research: Space Physics*, *119*(7), 5295–5304, doi:10.1002/2014JA020029.
- 508 Robinson, R. M., R. R. Vondrak, K. Miller, T. Dabbs, and D. Hardy (1987), On calculating iono-
509 spheric conductances from the flux and energy of precipitating electrons, *Journal of Geophysical*
510 *Research (Space Physics)*, *92*, 2565–2569, doi:10.1029/JA092iA03p02565.
- 511 Skopke, N. (1966), A General Relation between the Energ of Trapped Particles and the Disturbance
512 Field near the Earth, *J. Geophys. Res.*, *71*, 3125–3130, doi:10.1029/JZ071i013p03125.
- 513 Sergeev, V. A., and B. B. Gvozdevsky (1995), Mt-index: a possible new index to character-
514 ize the magnetic configuration of magnetotail, *Annales Geophysicae*, *13*(10), 1093–1103, doi:
515 10.1007/s00585-995-1093-9.
- 516 Sergeev, V. A., M. Malkov, and K. Mursula (1993), Testing the isotropic boundary algorithm
517 method to evaluate the magnetic field configuration in the tail, *Journal of Geophysical Research:*
518 *Space Physics*, *98*(A5), 7609–7620, doi:10.1029/92JA02587.
- 519 Serggeev, A. V., Sazhina, M. E., A. N., Lundblad, A. J., and Soraas (1983), Pitch-angle scattering
520 of energetic protons in the magnetotail current sheet at the dominant source of their isotropic
521 precipitation into the nightside ionosphere, *Planetary and Space Science*, *31*(10), 1147–1155.
- 522 Spasojevic, M., and S. A. Fuselier (2009), Temporal evolution of proton precipitation associated
523 with the plasmaspheric plume, *Journal of Geophysical Research: Space Physics*, *114*(A12), doi:
524 10.1029/2009JA014530.

- 525 Spasojevic, M., H. U. Frey, M. F. Thomsen, S. A. Fuselier, S. P. Gary, B. R. Sandel, and U. S.
 526 Inan (2004), The link between a detached subauroral proton arc and a plasmaspheric plume,
 527 *Geophysical Research Letters*, *31*(4), doi:10.1029/2003GL018389.
- 528 Sraas, F., J. . Lundblad, and B. Hultqvist (1977), On the energy dependence of the ring current
 529 proton precipitation, *Planetary and Space Science*, *25*(8), 757–763.
- 530 Tsyganenko, N. A. (1982), Pitch-angle scattering of energetic particles in the current sheet of the
 531 magnetospheric tail and stationary distribution functions, *Planetary and Space Science*, *30*(5),
 532 433–437.
- 533 Vasyliunas, V. M. (1970), Mathematical Models of Magnetospheric Convection and Its Coupling
 534 to the Ionosphere, in *Particles and Field in the Magnetosphere, Astrophysics and Space Science*
 535 *Library*, vol. 17, edited by B. M. McCormack and A. Renzini, p. 60.
- 536 Yahnin, A., and T. Yahnina (2007), Energetic proton precipitation related to ion cyclotron
 537 waves, *Journal of Atmospheric and Solar-Terrestrial Physics*, *69*(14), 1690 – 1706, doi:
 538 <https://doi.org/10.1016/j.jastp.2007.02.010>, pc1 Pearl Waves: Discovery, Morphology and
 539 Physics.
- 540 Yahnina, T. A., and A. G. Yahnin (2014), Proton precipitation to the equator of the isotropic
 541 boundary during the geomagnetic storm on november 20–29, 2003, *Cosmic Research*, *52*(1),
 542 79–85, doi:10.1134/S0010952514010092.
- 543 Young, D. T., H. Balsiger, and J. Geiss (1982), Correlations of magnetospheric ion composition
 544 with geomagnetic and solar activity, *Journal of Geophysical Research: Space Physics*, *87*(A11),
 545 9077–9096, doi:10.1029/JA087iA11p09077.
- 546 Young, S. L., R. E. Denton, B. J. Anderson, and M. K. Hudson (2002), Empirical model for
 547 scattering caused by field line curvature in a realistic magnetosphere, *Journal of Geophysical*
 548 *Research: Space Physics*, *107*(A6), SMP 3–1–SMP 3–9, doi:10.1029/2000JA000294.
- 549 Young, S. L., R. E. Denton, B. J. Anderson, and M. K. Hudson (2008), Magnetic field line curvature
 550 induced pitch angle diffusion in the inner magnetosphere, *Journal of Geophysical Research: Space*
 551 *Physics*, *113*(A3), doi:10.1029/2006JA012133.

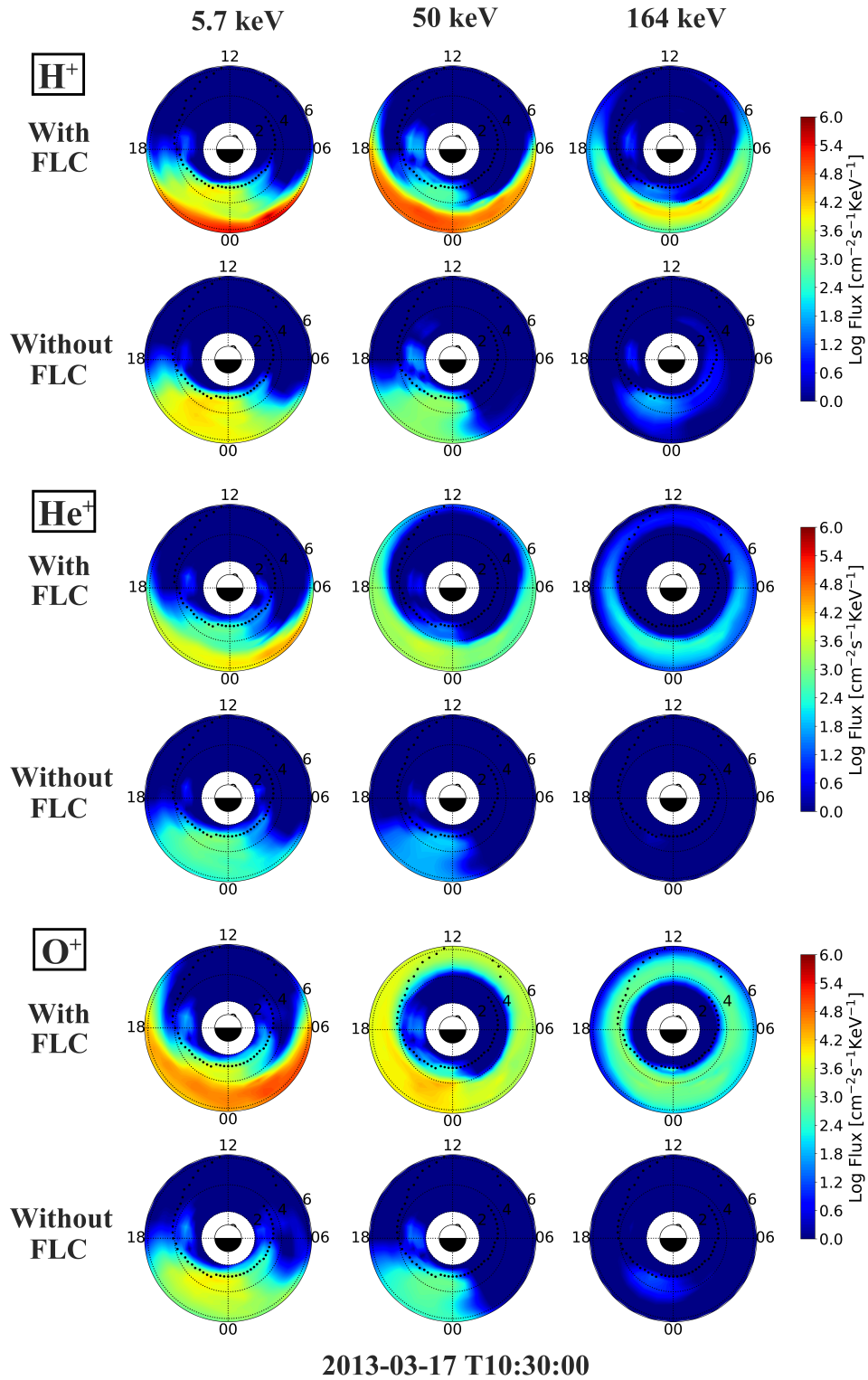
- 552 Yu, Y., V. K. Jordanova, A. J. Ridley, G. Toth, and R. Heelis (2017), Effects of electric field methods
553 on modeling the midlatitude ionospheric electrodynamics and inner magnetosphere dynamics,
554 *Journal of Geophysical Research: Space Physics*, *122*(5), 5321–5338, doi:10.1002/2016JA023850,
555 2016JA023850.
- 556 Yu, Y., X. Tian, and V. Jordanova (2020), Ram-scb simulation outputs, doi:
557 10.5281/zenodo.3631152.
- 558 Yue, C., C.-P. Wang, L. Lyons, J. Liang, E. F. Donovan, S. G. Zaharia, and M. Hender-
559 son (2014), Current sheet scattering and ion isotropic boundary under 3-d empirical force-
560 balanced magnetic field, *Journal of Geophysical Research: Space Physics*, *119*(10), 8202–8211,
561 doi:10.1002/2014JA020172.
- 562 Yue, C., J. Bortnik, W. Li, Q. Ma, C.-P. Wang, R. M. Thorne, L. Lyons, G. D. Reeves, H. E. Spence,
563 A. J. Gerrard, M. Gkioulidou, and D. G. Mitchell (2019), Oxygen ion dynamics in the earth’s
564 ring current: Van allen probes observations, *Journal of Geophysical Research: Space Physics*,
565 *124*(10), 7786–7798, doi:10.1029/2019JA026801.
- 566 Zaharia, S., C. Cheng, and K. Maezawa (2004), 3-D force-balanced magnetospheric configurations,
567 *Annales Geophysicae*, *22*, 251–265, doi:10.5194/angeo-22-251-2004.
- 568 Zaharia, S., V. K. Jordanova, M. F. Thomsen, and G. D. Reeves (2006), Self-consistent modeling
569 of magnetic fields and plasmas in the inner magnetosphere: Application to a geomagnetic storm,
570 *Journal of Geophysical Research (Space Physics)*, *111*, A11S14, doi:10.1029/2006JA011619.



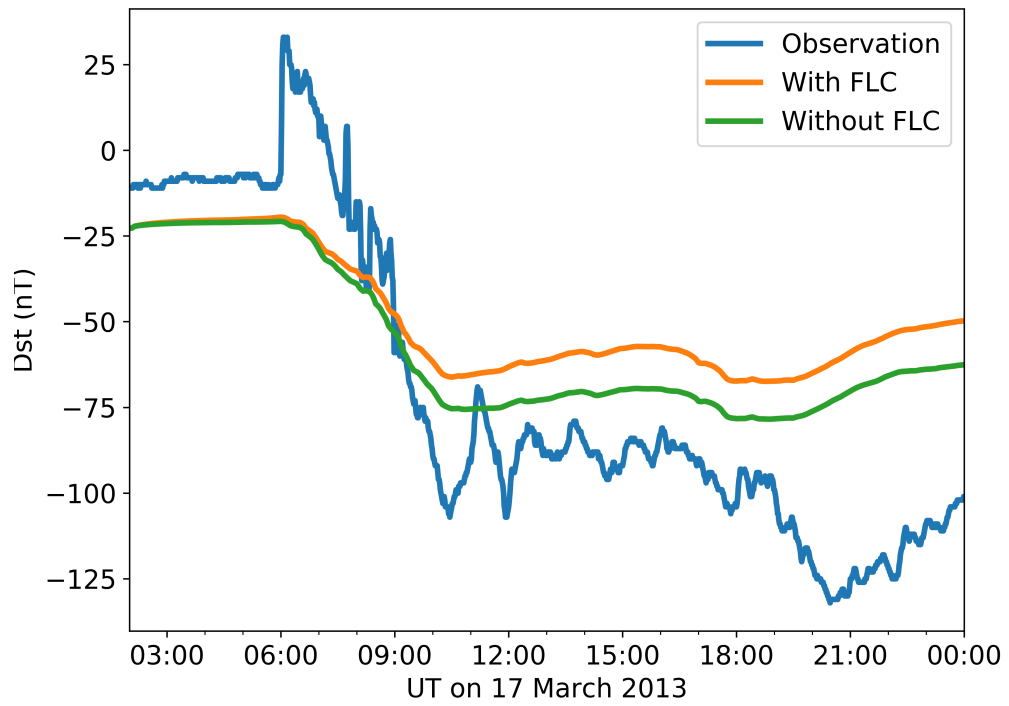
571 **Figure 1.** The solar wind, interplanetary, and geomagnetic conditions on the March 17, 2013
 572 storm event.



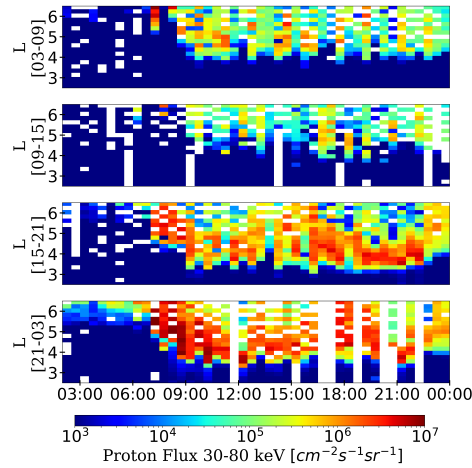
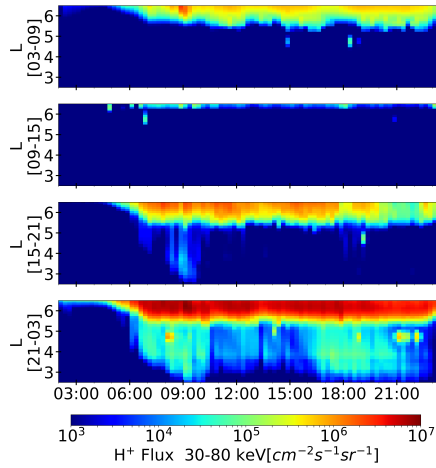
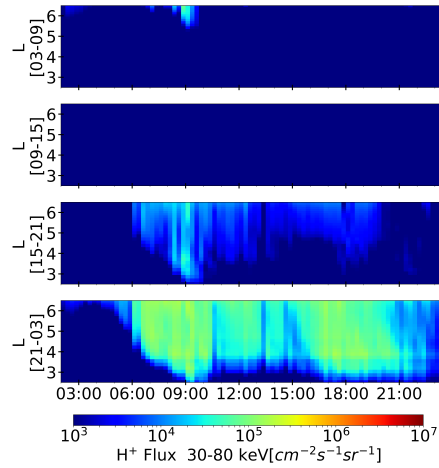
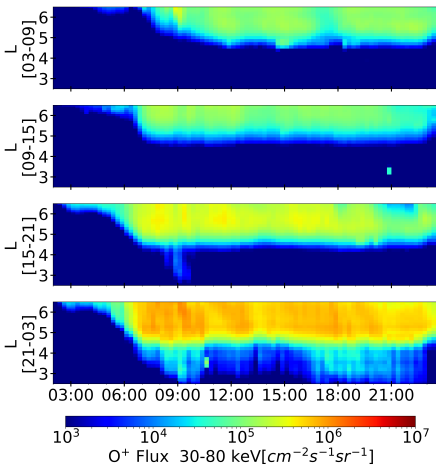
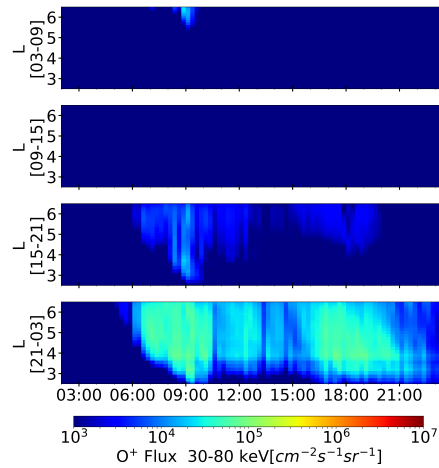
573 **Figure 2.** Left column: the rigidity parameter $\varepsilon = R_g/R_c$ for ions with $E=50\text{keV}$ and pitch
 574 angle of 50° . Middle column: diffusion coefficient $D_{\alpha\alpha}$ for field line scattering at $E=50\text{keV}$ and
 575 pitch angle of 50° in the equatorial plane. Right column: The diffusion coefficient as a function of
 576 energy and pitch angle at $\text{MLT} = 24$ and $L=6.5$. Different rows represent different ion species.



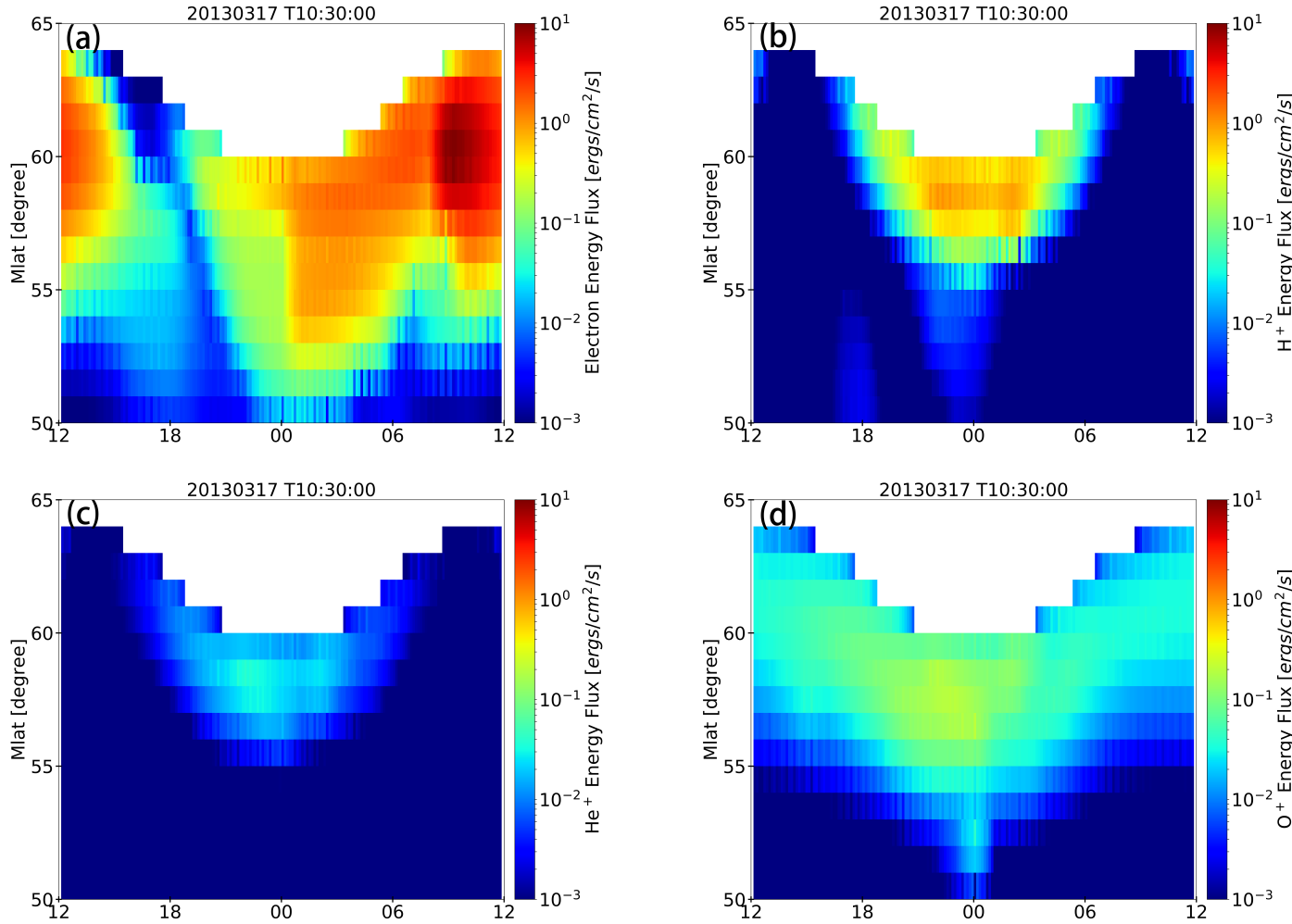
577 **Figure 3.** The global distribution of ion precipitating flux in the equatorial plane at different
 578 energies ($E=5.7, 50,$ and 164 keV). For each ion species, the precipitation distribution is compared
 579 between two simulations: with FLC scattering included and excluded.



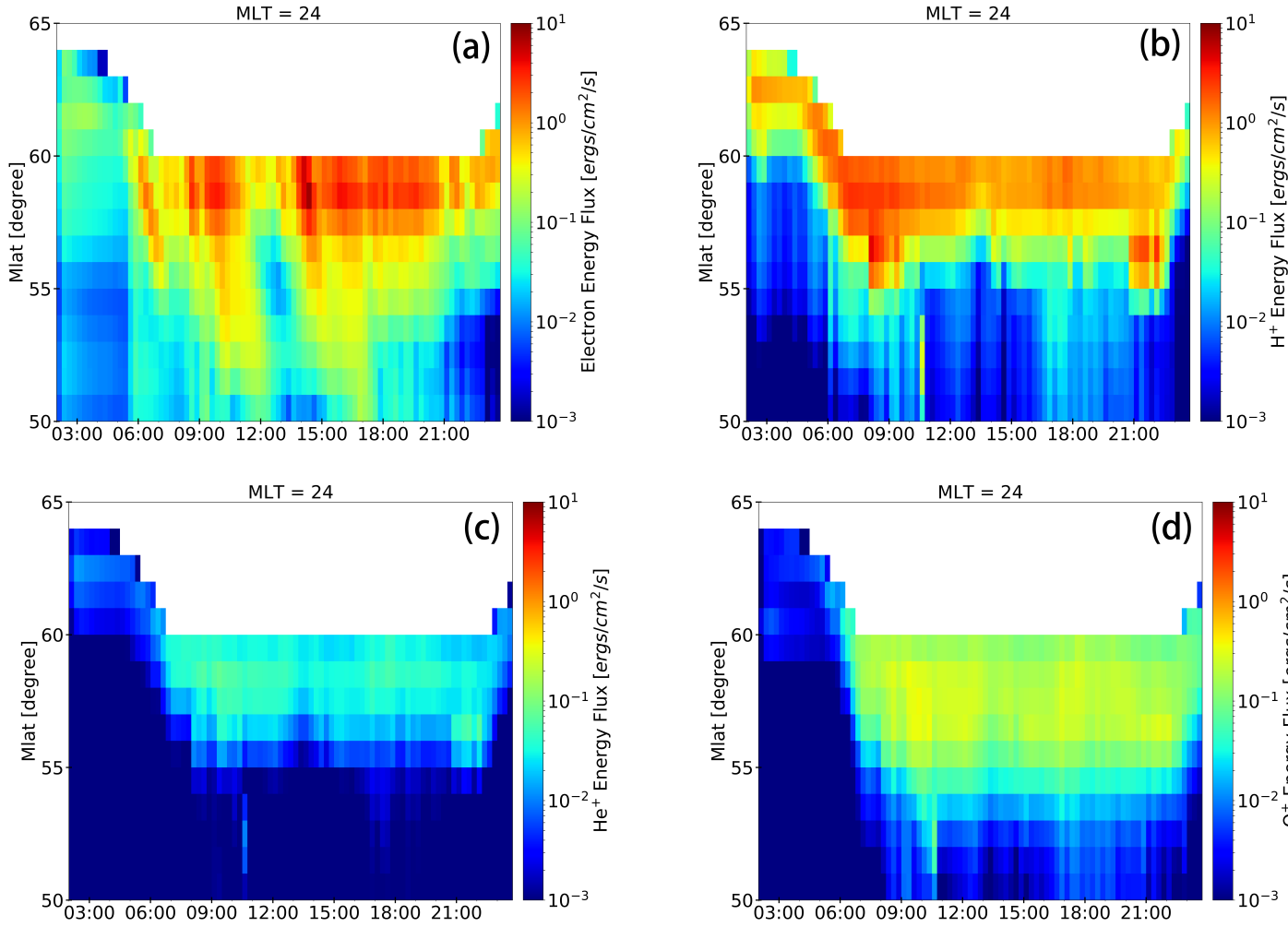
580 **Figure 4.** Dst index comparison between the observed SYM-H index and estimated index from
581 two simulations: with the FLC scattering included and excluded.

(a) POES observation (H^+ precipitation)(b) With FLC (H^+ precipitation)(c) Without FLC (H^+ precipitation)(d) With FLC (O^+ precipitation)(e) Without FLC (O^+ precipitation)

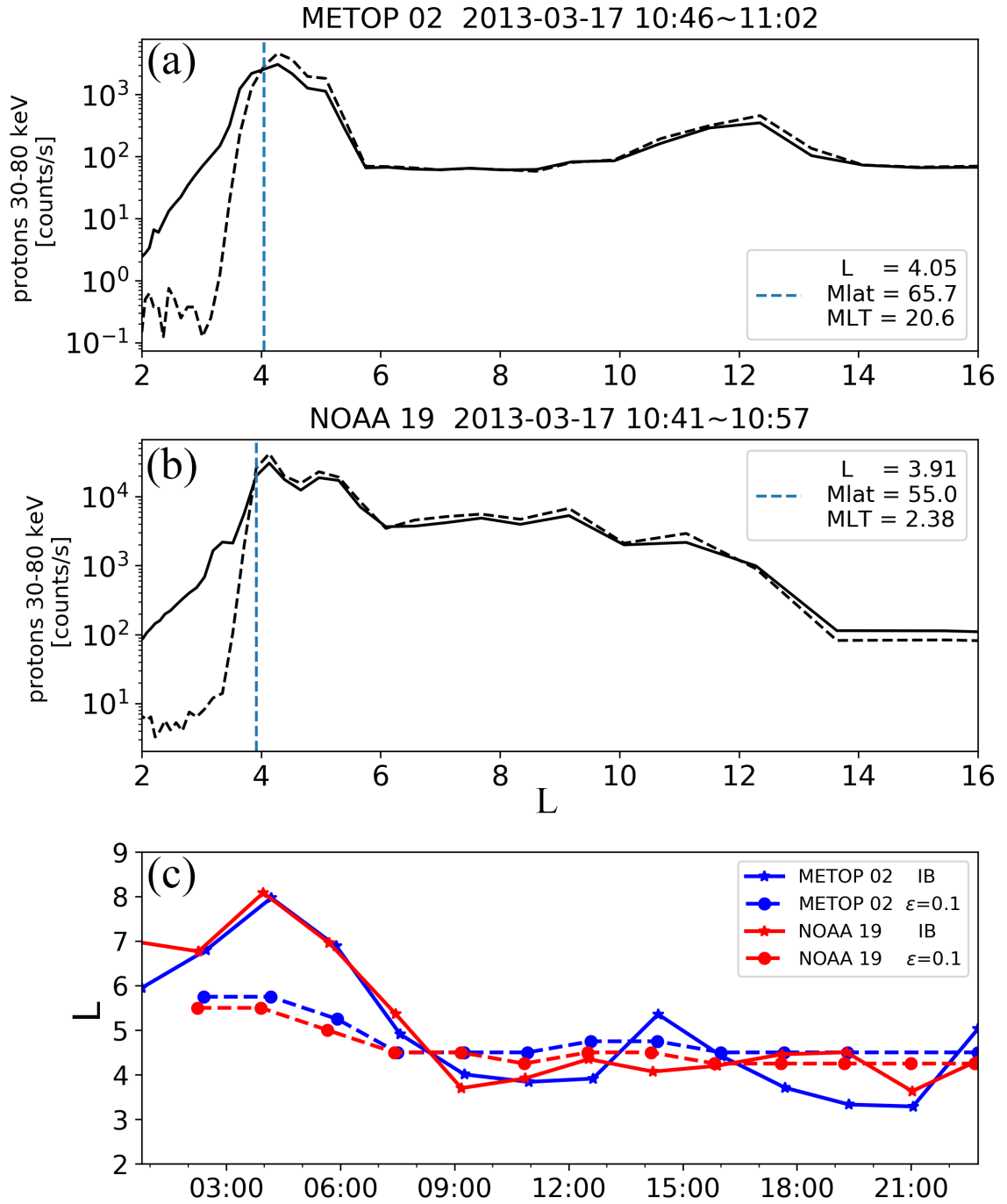
582 **Figure 5.** (a) Proton precipitating flux ($30 < E < 80$ keV) from POES observations at four different MLT sectors as a
 583 function of radial distance from the Earth and time. (b) The simulation results of proton precipitating flux with the FLC
 584 scattering included. (c) The simulation results of proton precipitating flux without the FLC scattering. (d) The simulation
 585 results of O^+ precipitating flux with the FLC scattering. (e) The simulation results of O^+ precipitating flux without
 586 the FLC scattering.



587 **Figure 6.** Spatial distribution of precipitating energy flux in the ionosphere at 10:30 UT, con-
 588 tributed respectively by (a) electron precipitation, (b) proton precipitation, (c) helium ion precipi-
 589 tation, and (d) oxygen ion precipitation. The energy flux is obtained by integrating differential flux
 590 over $150 \text{ eV} < E < 400 \text{ keV}$.



591 **Figure 7.** Temporal evolution of precipitating energy flux on the ionospheric midnight
 592 (MLT=24), contributed respectively by (a) electron precipitation, (b) proton precipitation, (c)
 593 helium ion precipitation, and (d) oxygen ion precipitation. The energy flux is obtained by integrating
 594 differential flux over $150 \text{ eV} < E < 400 \text{ keV}$.



595 **Figure 8.** (a, b) Two examples of determining the isotropic boundary from Metop02 and NOAA
 596 19 satellites. Dashed black line represents the precipitating proton flux observed by 0° telescope,
 597 and solid black line represents the trapped proton flux observed by 90° telescope. (c) Comparisons
 598 of the isotropic boundary location between the observations (solid lines) and simulations (dashed
 599 lines).